Materials Science & Engineering A 835 (2022) 142695

Contents lists available at ScienceDirect

Materials Science & Engineering A

journal homepage: www.elsevier.com/locate/msea

Evolution of microstructure and mechanical properties in 2205 duplex stainless steels during additive manufacturing and heat treatment

Nima Haghdadi [a,*], Carina Ledermueller [a], Hansheng Chen [b,c], Zibin Chen [b,c,d], Qian Liu [e], Xiaopeng Li [e], Gregory Rohrer [f], Xiaozhou Liao [b,c], Simon Ringer [b,c], Sophie Primig [a,**]

[a] School of Materials Science & Engineering, UNSW Sydney, Sydney, NSW 2052, Australia
[b] Australian Centre for Microscopy & Microanalysis, The University of Sydney, Sydney, NSW 2006, Australia
[c] School of Aerospace, Mechanical and Mechatronic Engineering, The University of Sydney, Sydney, NSW 2006, Australia
[d] Department of Industrial and Systems Engineering, The Hong Kong Polytechnic University, Hong Kong, China
[e] School of Mechanical and Manufacturing Engineering, The University of New South Wales (UNSW Sydney), Sydney, NSW 2052, Australia
[f] Department of Materials Science and Engineering, Carnegie Mellon University, Pittsburgh, PA, 15213-3890, USA

ARTICLE INFO

Keywords:
Additive manufacturing
Duplex stainless steel
Microstructure
Mechanical properties
Heat treatment

ABSTRACT

Metal additive manufacturing (AM) offers exceptional design freedom, but its high thermal gradients often generate non-equilibrium microstructures with chemical and interfacial instabilities. Steels that solidify as δ-ferrite often experience a further solid-state phase transformation to austenite during AM. The detailed nature of this phase transformation during AM is yet to be fully understood. Duplex stainless steel, which is known for its unique combination of high corrosion resistance and mechanical properties, is a suitable alloy to further study this phase transformation.

The current study aims to gain novel insights into solid-state phase transformations and mechanical properties of duplex stainless steels during laser powder-bed fusion (LPBF). As-printed microstructures exhibit significant deviations when compared to conventionally manufactured counterparts in terms of phase balance and morphology, elemental partitioning, and interface character distribution. During LPBF, only a small fraction of austenite forms, mostly at the ferrite-ferrite grain boundaries, via a phase transformation accompanied by diffusion of interstitials. Austenite/ferrite boundaries are shown to terminate on $\{100\}_F//\{111\}_A$ planes. This is due to the character of parent ferrite-ferrite boundaries which is dictated by the sharp <100> texture and geometry of austenite grains induced by directional solidification and epitaxial growth of ferrite. Benchmarking mechanical properties against a wrought counterpart demonstrates that AM offers high strength but relatively low ductility and impact toughness. A short heat treatment reverts the microstructure back to its equilibrium state resulting in balanced tensile and toughness properties, comparable to or even better than those of wrought counterparts.

1. Introduction

Duplex stainless steels (DSSs) are designed to synergistically combine the superior properties of ferrite and austenite to achieve advanced mechanical and corrosion properties [1]. These steels solidify initially as δ-ferrite, which partially transforms to austenite upon cooling to temperatures lower than ~1370 °C. Control of the chemical composition and the ferrite-to-austenite phase transformation path are the main means to adjust the volume fraction, morphology, and chemistry of the two phases [2–4]. Traditionally, roughly equal fractions of austenite and ferrite are considered as the optimum phase balance, and steels with such microstructures are widely used in harsh environments such as in offshore infrastructures e.g., for oil and gas industries, paper and pulp industries, and desalination plants [1]. Although the majority of duplex steel parts currently in use are manufactured via casting and forming, there are currently ongoing efforts to employ alternative state-of-the-art manufacturing processes such as 'additive manufacturing' to fabricate DSS components. DSSs have a low thermal expansion coefficient and relatively high thermal conductivity compared to austenitic stainless steels, making them fit for additive

* Corresponding authors.
** Corresponding authors.
E-mail addresses: nima.haghdadi@unsw.edu.au (N. Haghdadi), s.primig@unsw.edu.au (S. Primig).

https://doi.org/10.1016/j.msea.2022.142695
Received 25 November 2021; Received in revised form 16 January 2022; Accepted 17 January 2022
Available online 20 January 2022
0921-5093/© 2022 Elsevier B.V. All rights reserved.

manufacturing of complex and thin-walled geometries e.g., as heat exchangers [5].

Additive manufacturing of metals, although offering remarkable design freedom, has its own challenges in terms of reliably predicting microstructure–property relationships. Steep thermal gradients and complex thermal cycles result in microstructural heterogeneities and instabilities [6–8]. This is exacerbated in the case of many of steels where, in addition to solidification, the material undergoes solid-state phase transformations e.g., δ-ferrite to austenite and/or austenite to ferrite/bainite/martensite transformations. While the feasibility of additive manufacturing of steels with advanced properties is well established [9], there are still considerable knowledge gaps on the phase transformation as well as the elemental partitioning and interface crystallographic character evolution during solid state transformations. One example where this unsatisfactory state of knowledge exists is in duplex stainless steel, a material that besides its technological importance, can be considered as a model alloy to study the δ-ferrite (referred to as ferrite in the following) to austenite phase transformation.

DSSs have so far mainly been additively manufactured via laser powder bed fusion (LPBF) and directed energy deposition (DED) techniques [10–15]. DSS fabricated by LPBF has a mostly (>95%) ferritic structure, while DSS fabricated by DED has a relatively lower volume fraction of ferrite. This is mainly due to the higher cooling rate in LPBF, and the significant 'intrinsic' annealing that the material experiences and the use of filler metal during process during DED [14]. Considering the dominance of ferrite in the LPBF steel, a supersaturation of nitrogen (N) in the ferrite matrix has been reported to cause the precipitation of chromium nitride [11,15]. This leads to a higher strength but reduced ductility in LPBF DSS compared to traditionally manufactured DSS [11]. An annealing treatment at ~1000 °C has been proposed to restore the austenite-ferrite balance and the corresponding ductility properties [11, 15]. Despite these contributions, several aspects of the microstructural evolution and mechanical properties of AM DSS yet remain unclear:

While there are reports on the effect of cooling rate (e.g., furnace cooling, air cooling and water quenching) on the phase transformation mechanisms, austenite morphology and interface character in DSS [3, 16,17], such knowledge for the high cooling rates associated with LPBF is lacking. Furthermore, despite previous reports on the high strength of the DSS in LPBF state and the recovery of ductility by annealing [11], there is a lack of data on the impact toughness of these steels after LPBF. Crack initiation and propagation predominantly occur in the ferrite with the austenite phase acting as a barrier to crack growth [18]. The toughness of DSS is, therefore, dependent on the partitioning of load between austenite and ferrite. This is governed by the chemistry and strength of each phase, grain size and morphology, and interface character [19,20]. LPBF DSS are expected to show distinct characteristics with regards to all of these features when compared to traditional DSS, with opportunities on offer to tune the microstructure and thus impact toughness and other properties via adjusting printing parameters.

The purpose of this study is to determine if DSSs fabricated by AM have interface distributions, phase balance and mechanical behavior similar to or distinct from the same steel when conventionally processed. To answer this question, we examined a DSS processed by LPBF in the as-built condition and after a post-AM anneal using a variety of characterization tools (e.g., electron backscatter diffraction (EBSD), electron probe micro-analysis (EPMA), (scanning) transmission electron microscopy ((S)TEM), and atom probe tomography (APT)) and mechanical tests (i.e., tensile and impact toughness). The results indicate that the LPBF steel has an aboundance of Cr-rich nitrides, a low austenite fraction and an unusual austenite-ferrite orientation relationship (OR) that is created by the texture and geometry of grains imposed by AM process. During annealing, nitrides dissolve, more of the ferrite transforms to austenite and the OR becomes consistent with conventional processing. It is also noted that while AM offers very high tensile strength, a post-AM annealing is required for applications where high ductility and impact toughness are needed.

2. Material and methods

2.1. Material, LPBF and heat treatment

2205 DSS powder was purchased from Sandvik Osprey Ltd, with the chemical composition of 0.02C, 22.60 Cr, 5.90 Ni, 1.10 Mn, 3.20 Mo, 0.02 P, 0.6 Si, 0.18 N, 0.01 S (in wt%), and balance of Fe. The particle size for the powders was in the range of 15–53 μm (measured via sieve and laser diffraction analyses), and the particles were mostly of a spherical morphology (Supplementary Fig. 1). The specimens were printed in a SLM Solution 125^{HL} machine, equipped with a 400 W continuous wavelength fibre laser (1060 nm), under an Ar gas atmosphere (i.e., <200 ppm O during the entire process), using a 316 stainless steel substrate. The substrate was pre-heated to 200 °C. Cubic samples with geometries of 15 × 15 × 15 mm^3 (for microstructural analysis), 55 × 5 × 10 mm^3 (for Charpy impact toughness testing in accordance with ASTM E23-07a), and in line with Standard ASTM E8/E8M for tensile testing were printed. Optimised printing parameters were selected as follows; laser power: 200 W, scan speed: 700 mm/s, hatch spacing: 60 μm, layer thickness: 30 μm, and an incremental 67° rotation was implemented after each layer. In order to gain a higher volume fraction of austenite, some samples were heat treated at 1000 °C for 10 min. This temperature was selected based on previous studies on the same steel to maximise the austenite fraction [11], while avoiding formation of any undesirable secondary phases [21]. This short heat treatment was conducted in an Ar atmosphere using a muffle furnace, and the samples were water quenched after annealing.

2.2. Microscopy

2.2.1. Optical and scanning electron microscopy

Optical microscopy (OM) was conducted using Olympus TM BX53MRF-S. Samples were first ground to 1200 grit, then polished down to a 1 μm diamond suspension. They were then etched using Carpenter's reagent for 5 s. The images were taken on the zx surfaces (z being the build direction). The fracture surfaces of the tensile and Charpy samples were studied via scanning electron microscopy (SEM) in the secondary electron mode in a Zeiss Auriga SEM at 15 kV with an aperture size of 30 μm.

2.2.2. EBSD and EPMA

EBSD analyses were carried out using a JEOL 7001F SEM equipped with a Hikari 31 Super EBSD Camera. EBSD sample were fine polished using 0.04 μm OPU colloidal silica. Initial EBSD scans were performed at different sites along the build height. Since there were no significant differences observed, further EBSD analyses were confined to the middle height of each sample. An accelerating voltage of 25 kV, a probe current of 14 nA, a 6 × 6 binning, and step sizes of 1 and 0.1 μm were used for EBSD analyses. The TSL-OIM software was used for data collection and analysis. Supplementary Fig. 2 gives an overview image of the as-built and heat treated samples at different cross sections. Interphase boundaries habit planes were measured based on the method developed by Rohrer et al. [22]. A description of the method has been given in the Supplementary Material. EPMA was conducted using a JEOL JXA-8500F electron probe microanalyser equipped with wavelength dispersive spectrometer (WDS) detectors, operated at 15 kV and a probe current of 400 nA. X-ray intensity maps were generated with a step size of 100 nm and a dwell time of 20 ms/pixel, using the L_α line for Mo and K_α line for all other elements.

2.2.3. TEM

For the LPBF and post-LPBF heat-treated (LPBF + HT) samples, thin foils were prepared using electropolishing with a STRUERS Tenupol and a STRUERS A2 electrolyte at 26 V and ~-20 °C. For the TEM analysis of the sample after impact testing, the focussed ion beam (FIB) lift-out method was used. For this, a plasma FIB (ThermoFisher Helios G4 Xe)

was employed for the initial lift-out, and final thinning was done in a FEI Nova Nanolab 200 Gallium-FIB. (S)TEM analysis of thin foils using techniques including bright-field imaging, energy dispersive spectroscopy (EDS) and low angle annular dark field (LAADF) imaging was conducted using a Themis-Z double-corrected microscope at 300 kV.

2.2.4. APT

APT tips were prepared either by the standard electropolishing technique or the FIB-assisted site-specific lift-out technique from the mid height of the printed samples. Regarding the electropolishing technique, as-built samples were mechanically sectioned into blanks with dimensions of ~0.5 × 0.5 × 10–15 mm^3 with the blanks' length being aligned with the build direction. These blanks were roughly polished in a 25% perchloric acid under a voltage of ~20 V at room temperature, and then annularly milled in a Xe plasma FIB-SEM (Thermofisher G4) or a Gallium focussed ion beam-scanning electron microscopy (FIB-SEM, Zeiss Auriga) under 30 kV. Finally, all tips were annularly milled with lower voltages to remove the damaged surface layers. For the site-specific lift-out technique, the Xe plasma FIB-SEM was used to prepare a needle-shaped APT tip containing a ferrite-ferrite grain boundary following procedures described elsewhere [23].

APT experiments were conducted in a CAMECA Local Electrode Atom Probe (LEAP) 4000X Si equipped with a picosecond-pulse ultraviolet laser (laser frequency = 200 kHz, laser pulse energy = 50 pJ). The base temperature was maintained at ~50 K. APT data reconstruction was performed via Cameca's Integrated Visualization & Analysis Software (IVAS) version 3.8.4 [24]. The values of detector efficiency, image compression factor (ICF), and field factor (k_f) were set as 0.57, 1.65, and 3.30 for APT data reconstruction. The bin width was 0.3 nm.

2.3. Mechanical testing

Tensile samples were printed into flat, dog-bone shapes with the dimensions of 4 mm width, 2 mm thickness and 20 mm gauge length. Tensile testing was performed in an Instron 5982 tensile testing machine equipped with an MTS laser extensometer Lx500. Tests were conducted at a constant crosshead speed of 1 mm/min at room temperature and an average of 2–3 samples were tested for each condition. For impact toughness testing, subsize V-notch samples were printed according to ASTM E23-07a, with 55 mm length and 10 × 5 mm^2 cross sections. Two sets of samples were printed with one having the build direction aligned with the 55 mm length dimension, and the other aligned with the 10 mm dimension. Impact tests were performed at two temperatures of RT and −110 °C using a Mohr & Federhaff A.G. pendulum impact testing machine, with the temperature being monitored using a K-type thermocouple spot welded onto the samples. An average of 2–3 samples were used to obtain the impact energy for each condition. Note that for benchmarking purposes, tensile properties of a wrought (hot rolled) 2205 DSS with the chemical composition of 0.036C, 0.321 Si, 1.82 Mn, 0.013 P, 23.2 Cr, 5.6 Ni, 2.90 Mo, 0.034 Co, 0.153 Cu, 0.245 N, and balance of Fe (in wt %) was also examined.

3. Results

3.1. As-built (LPBF) microstructure

Optical micrographs of the as-built (LPBF) samples (Fig. 1) show that the microstructure consists of grains elongated along the build direction. Based on their crystallographic orientation, grains show distinct reactions to etching revealing the location of grain boundaries. At higher magnification, the locations of melt pool boundaries within the microstructure become evident (shown by yellow arrows in Fig. 1b). There is a ~30 μm distance between individual melt pool boundaries along the build direction. Grains are, however, observed to be extended across several melt pools, indicating an epitaxial growth mechanism.

Fig. 2a–h shows the microstructure and interface characateristsics of the LPBF sample. EBSD mapping reveals that the microstructure after LPBF is mostly ferritic with only ~2% austenite usually observed as allotriomorphic thin layers located at ferrite-ferrite grain boundaries (Fig. 2a,d,e,f). Austenite particles are not randomly dispersed across ferrite-ferrite boundaries, and are usually seen only in particular locations, most likely in regions close to melt pool boundaries. This is in line with our recent observations in an LPBF 17–4 PH steel with a microstuture similarly consisting of austenite and ferrite [25]. Interestingly, most of austenite particles are elongated either parallel or perpendicular to the BD. Ferrite shows a strong <100> texture parallel to the BD (Fig. 2b), and ferritic grains are usually elongated, implying the dominance of epitaxial growth across several layers. An EPMA analysis of the LPBF sample (Fig. 3) reveals that no partitioning of substitutional elements occurs between austenite and ferrite, which means both phases have a composition far from the equilibrium in the as-LPBF condition. However, a partitioning of N and C towards austenite can be observed. It is interesting that thermal cycles inherent in LPBF have not been able to provide enough activation energy or time for substitutional atoms to diffuse to trigger partitioning.

The misorientation angle/axis distribution between austenite particles and the ferrite matrix (Fig. 2c) shows a peak at ~42–46°/<11 2 2> implying the dominance of both Kurdjomov-Sachs (KS) and Nishiyama-Wasserman (NW) orientation relationships. Using the stereological method explained in Ref. [22], the habit planes for the austenite-ferrite interfaces were measured for all the misorientations irrespective of angle/axis (Fig. 2g and h). It is observed that while austenite terminates on the expected {111} plane, ferrite deviates from the crystallographically and energetically expected {110} [3], and instead terminates on {100} planes. The austenite peak at {111} and the ferrite peak at {100} both are of a multiple random distribution (MRD) of ~3.0 implying that these planes exhibit populations three times higher than in a random distribution.

TEM imaging reveals that ferrite grains after LPBF show an elongated cellular structure and contain a high density of dislocations (Fig. 4). This

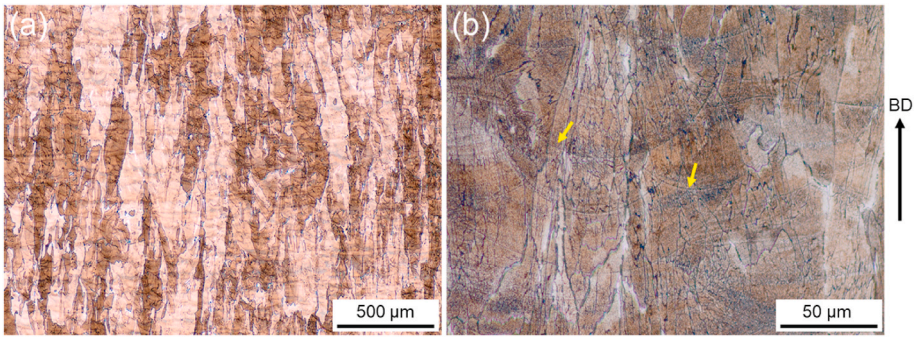

Fig. 1. (a, b) Typical optical micrographs of the duplex stainless steel samples processed by LPBF at two magnifications. Yellow arrows in (b) show examples of melt pool boundaries. BD indicates the build direction.

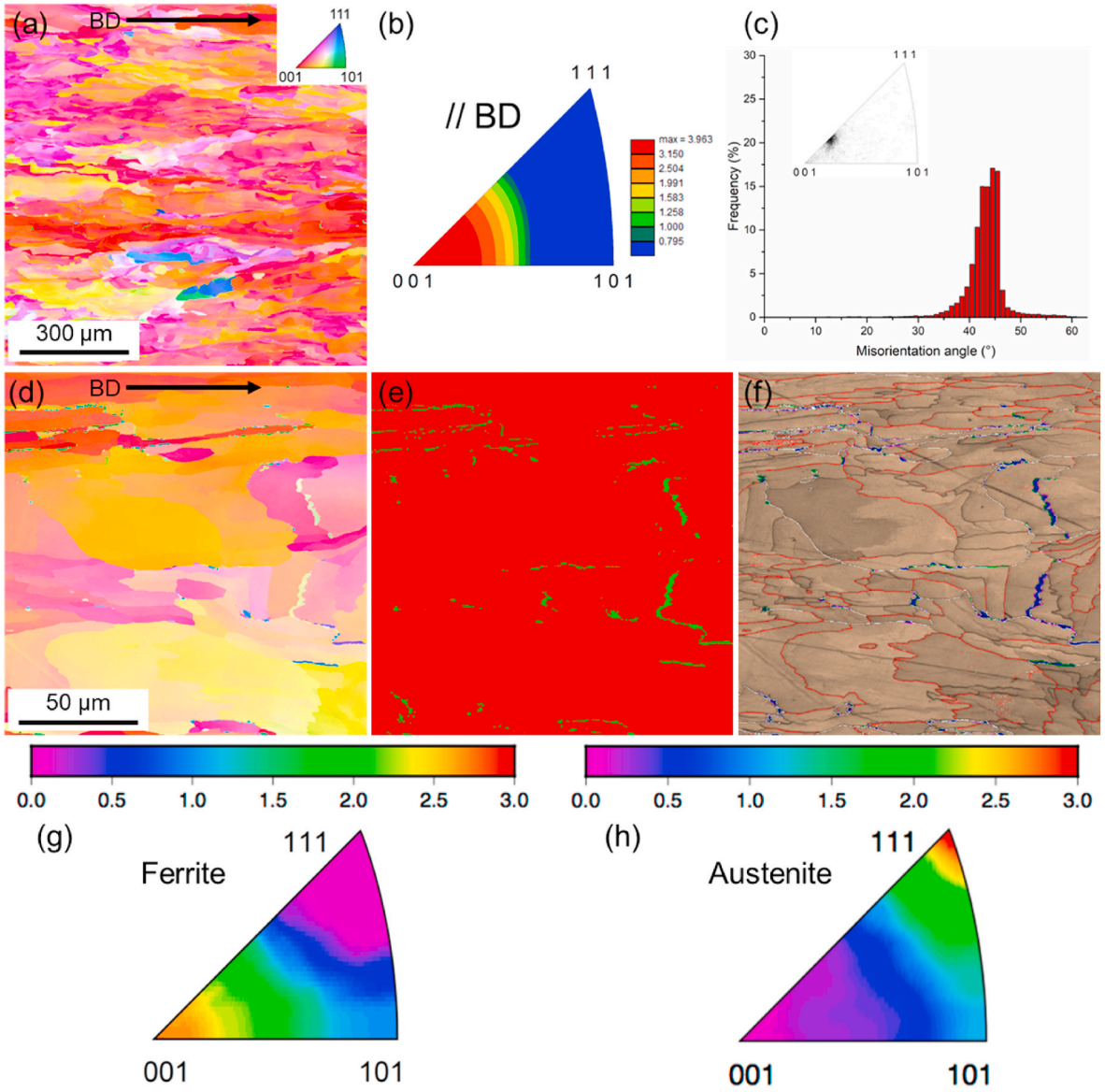

Fig. 2. (a) EBSD IPF map (along the build direction) taken from the central region of the LPBF DSS build. (b) Texture (IPF) of ferrite along the BD. (c) Misorientation angle between austenite and ferrite with the inset showing the misorientation axis at the angle of 42–46°. (d) Higher magnification IPF map of the same region in (a). (e) Phase map corresponding to (d) with ferrite coloured red and austenite coloured green. (f) Image quality map of the region in (d) and (e) with austenite coloured blue, white lines representing high angle boundaries ($\theta > 15°$) and red lines representing grain boundaries with $5° < \theta < 15°$. Magenta lines refer to Kurdjomov-Sachs (KS) and green lines refer to Nishiyama-Wasserman (NW) interfaces between austenite and ferrite. (g, h) Grain boundary habit plane distributions for ferrite and austenite in all austenite-ferrite boundaries irrespective of misorientation. 12,368 austenite/ferrite boundary segments were used to plot these heat maps. The colour keys show multiple random distribution (MRD).

is indicative of the development of plastic gradients within the grains that are accommodated via the formation of geometrically necessary dislocations [26]. There is a concentration of dislocations at the grain boundaries to accommodate the non-homogeneous slip therein [27] (see red arrows in Fig. 4b). In addition to these dislocations, the microstructure shows a high volume fraction of nano-scale particles. EDS mapping confirms that these particles are generally of two types; (i) enriched in Cr and N, and (ii) enriched in Si and O. This implies that these particles are chromium nitride (Cr_2N) and Si-rich oxides, respectively. Si–O inclusions can be from the powder feedstock or from the laser melting due to the high affinity of silicon for oxygen. The rapid cooling rates, in the order of what is typically experienced during LPBF, have been shown to produce amorphous oxygen inclusions in both duplex and single-phase stainless steels [28–30]. The spherical, rather than faceted, morphology of these inclusions in our study in particular implies an amorphous nature. The Cr_2N particles are seen in two modifications, intragranular and intergranular (Fig. 4c). Intergranular Cr_2N show a continuous morphology elongated along the grain boundaries while intragranular particles are dispersed within the matrix. Interestingly, a large number of the intragranular Cr_2N particles, that have either a rod-shape or a plate-like morphology, are formed adjacent to the silicon oxide particles (compare Si-rich regions to Cr-rich regions in EDS maps in Fig. 4c).

Dislocations are observed inside austenite grains also (Fig. 5a and b). Cr-rich and Si-rich regions can be detected in austenite too (Fig. 5c), though their relative volume fraction is considerably lower compared to that in ferrite. This is likely due to the higher supersaturation (due to lower solubility) of N and faster precipitation kinetics of elements in ferrite compared to austenite.

To further study the chemistry of nano-sized precipitates and

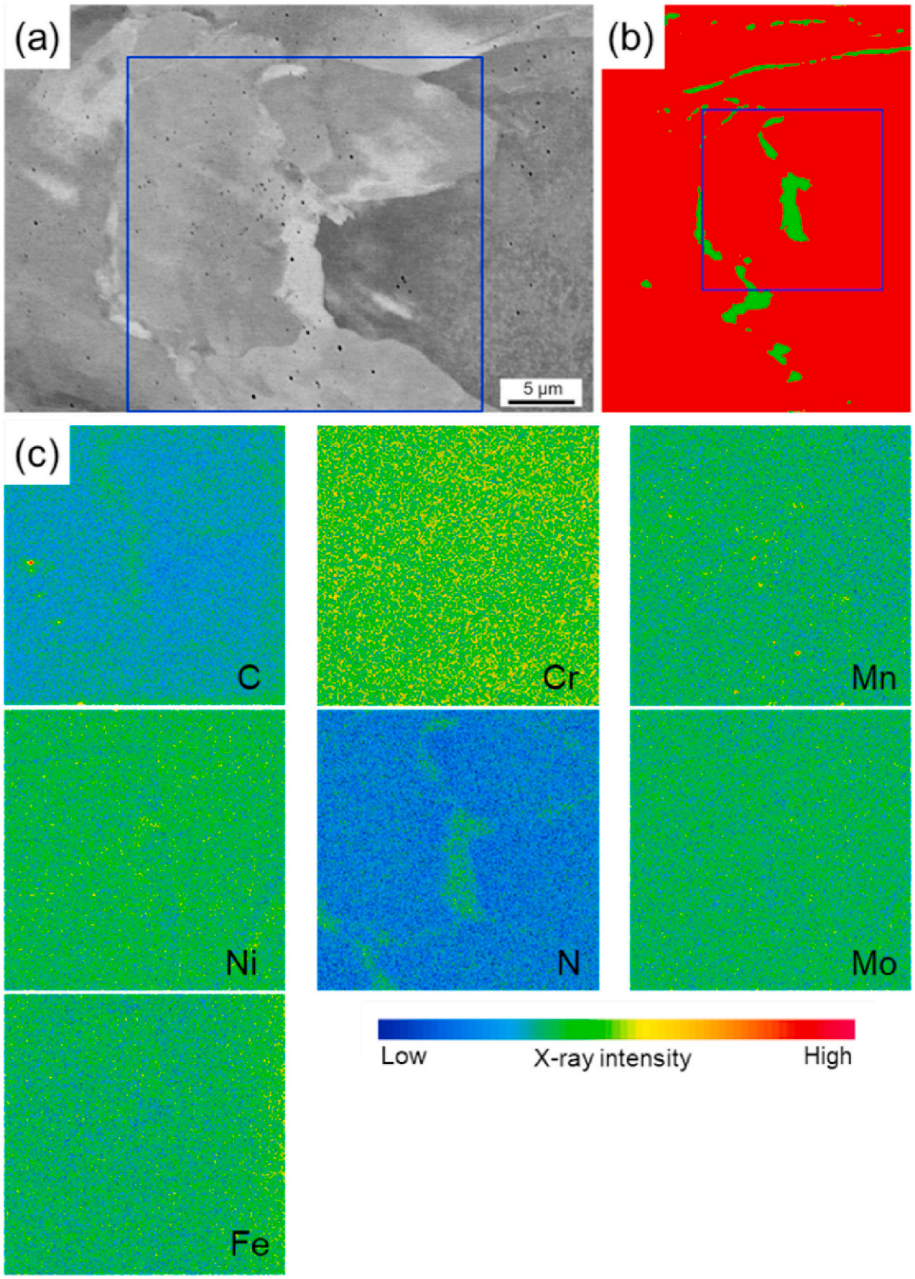

Fig. 3. (a) SEM image of the LPBF DSS, with blue square indicating the area of the EPMA maps, (b) EBSD phase map of the same region with ferrite in red and austenite in green. Blue square indicates area for EPMA mapping. (c) EMPA elemental maps of C, Cr, Mn, Ni, N, Mo, and Fe.

inclusions in the LPBF sample, APT was employed. Site-specific APT analysis of a high-angle ferrite-ferrite boundary reveals that Cr rich regions are expanded across the grain boundary, and that this film is sometimes penetrated by other particles, for example silicon oxides (Fig. 6). Across the width of the GB there is a ~12 nm depletion zone of Ni and Fe, enriched in Cr and N. This implies that this feature is either Cr_2N or the embryonic state of Cr_2N precipitates. There is also an increase in Mo and C at these regions, although at much lower concentrations.

Atom probe analysis of electro-polished tips provides insights into the chemistry of other features such as intragranular plate-like and rod-like Cr_2N regions (Fig. 7). It can be seen that in addition to N and Cr, there is a slight segregation of Mo into plate-like Cr_2N particles consistently across their width. Occasionally, there is also segregation of Si at selected interfaces between ferrite and Cr_2N, while this is not observed at other interfaces of the same kind. This gives strength to the idea of the formation of some Cr_2N particles adjacent to silicon oxides. APT also reveals that the segregation and depletion behavior of alloying elements at rod-like particles is weaker than that at plate-like particles. This is particularly clear for Mo and Ni (Fig. 7 c-e).

3.2. *Effect of post-LBPF heat treatment*

In order to achieve a close to balanced volume fraction of austenite, LPBF samples were heat treated at 1000 °C for 10 min. Fig. 8a–h shows the microstructure and interface characateristics of the sample after heat treatment. As can be seen in Fig. 8, after heat treatment, two different morphologies of austenite are formed. Relatively large austenite particles are observed at the initial ferrite-ferrite grain boundaries with an allotriomorphic morphology (shown by dashed rectangles in Fig. 8d). In addition, fine intragranular austenite grains (with an average size of ~2 μm) are dispersed inside the ferritic matrix. An EPMA analysis (Fig. 9)

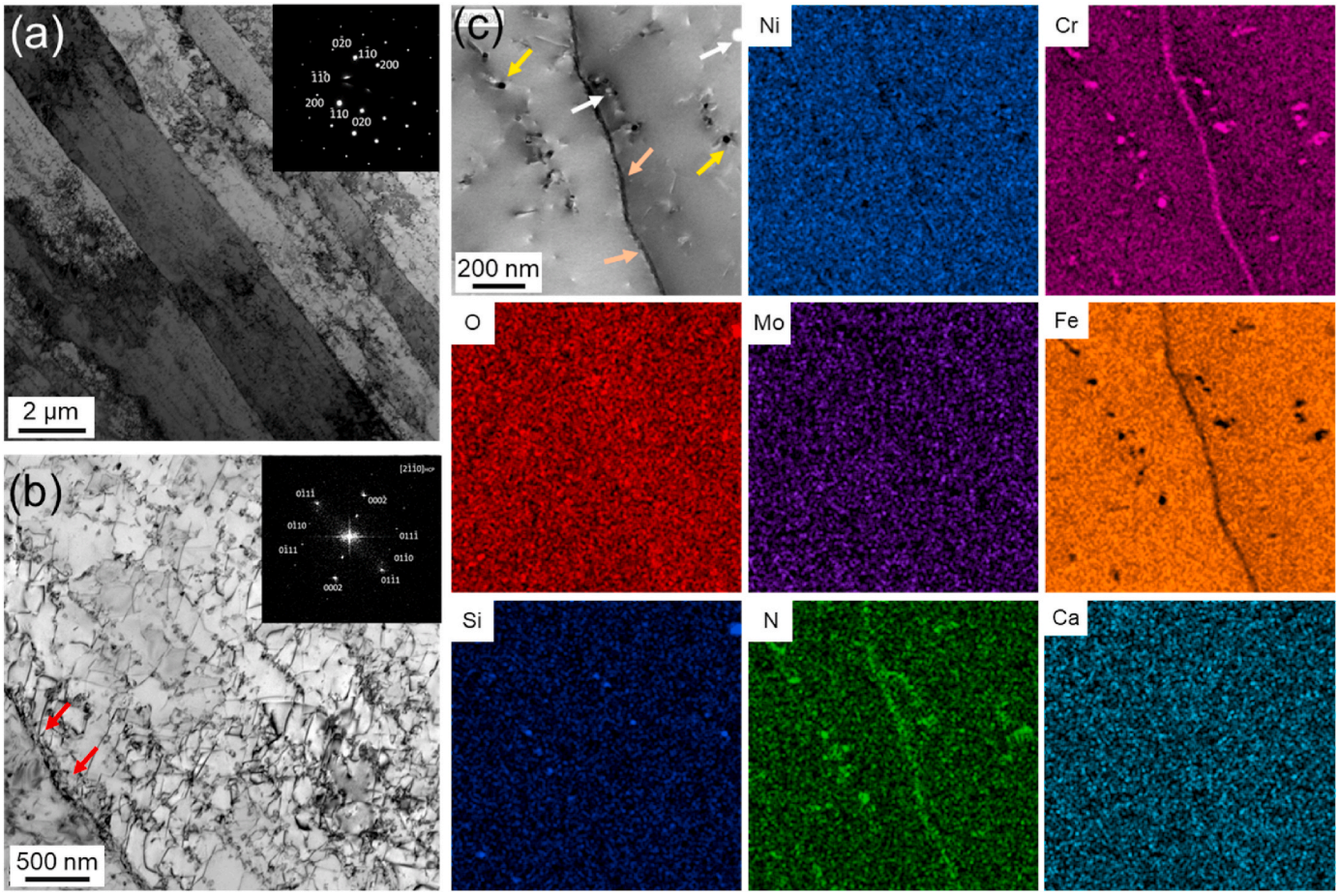

Fig. 4. (a) Bright field TEM image showing grain morphology and dislocations (inset showing SAD pattern of ferrite matrix). (b) Bright field TEM image showing dislocations and precipitates/particles (inset showing FFT pattern of a Cr_2N particle). (c) HAADF image and corresponding EDS maps for different elements with segregation in different phases. The Cr and N distribution maps reveal the location of the Cr_2N phase while the Si and O elemental maps reveal silicon oxide particles. Red arrows in (b) show examples of dislocation accumulation at the grain boundaries. Examples of Si–O (white arrows) and Cr_2N particles (intragranular: yellow arrows, and intergranular:orange arrows) are marked in (c).

shows that after the heat treatment, in contrast to the as-LPBF condition (see Fig. 3), there is a clear partitioning of substitutional alloying elements between austenite and ferrite. Mo and Cr partition into ferrite, and Ni and Mn into the austenite.

The misorientation angle/axis distribution of austenite/ferrite boundaries (Fig. 8c) exhibits a sharp peak at ~ 43° <5 1 1>. This implies that a significant volume fraction of interfaces are of KS character. An interface misorientation map (Fig. 8f) reveals that most of the intragranular austenite is of KS OR, while interfaces of random (irrational) ORs (austenite-ferrite interfaces that are neither magenta nor green in Fig. 8f) are mostly observed close to the parent ferrite-ferrite boundaries. The plane character distribution analysis of austenite-ferrite interfaces regardless of misorientation (Fig. 8g and h) shows that austenite peaks at the {111} position, and ferrite peaks at {110}. The austenite peak at {111} is of an MRD of 2.2 implying {111} planes are populated 120% more than expected in random distribution while the MRD for ferrite {110} planes is 1.4 showing 40% higher than random chances of ferrite planes terminating on {110} planes.

TEM analyses reveal that almost all the Cr_2N particles are dissolved during the heat treatment (LPBF + HT), while silicon oxide particles remain present in the microstructure (Fig. 10). The elemental partitioning revealed by TEM EDS is in line with the EPMA results with Fe and Ni partitioning to austenite and Cr and Mo to ferrite. In line with TEM results, we do not observe any Cr–N rich regions in the ferrite phase in the annealed sample in any of the APT tips studied.

3.3. Mechanical properties

Tensile testing and impact Charpy testing was carried out on both as-printed (LPBF) and heat treated (LPBF + HT) samples. The tensile properties were benchmarked against a conventionally wrought (hot rolled) sample (Fig. 11). The microstructure characteristics of the wrought DSS can be found in Supplementary Fig. 3.

The LPBF sample shows significantly higher tensile strength (yield strength (YS) = 651 ± 6 MPa and ultimate tensile strength (UTS) = 844 ± 5 MPa) compared to the wrought sample (YS = 493 ± 5 MPa and UTS = 709 ± 4 MPa). Ductility of the LPBF sample, however, is lower than the wrought sample (Elongation (EL%) of 18 ± 1 for the LPBF sample vs. EL% of 34 ± 2 for the wrought sample). LPBF followed by heat treatment (LPBF + HT) is shown to result in an optimum combination of tensile properties i.e., a YS of 563 ± 15 MPa and UTS of 798 ± 5 MPa, while demonstrating an acceptable level of 28 ± 2 EL%.

The fracture surfaces after tensile testing reveal that the mode of fracture changes for different samples. For the LPBF sample, where the microstructure is mostly ferritic, the fracture surface is of a mixed character with some areas showing brittle cleavage and the rest of the fracture surface exhibiting dimples (Fig. 11 b). For the wrought and LPBF + HT samples, however, an almost fully ductile fracture surface is observed where dimples are dominant (Fig. 11 c, d). Dimples seem to be larger in the wrought sample compared to the LPBF + HT sample. The fine dimples observed in the LPBF + HT sample can be correlated to the fine size of austenite particles (~2 μm) in this particular microstructure.

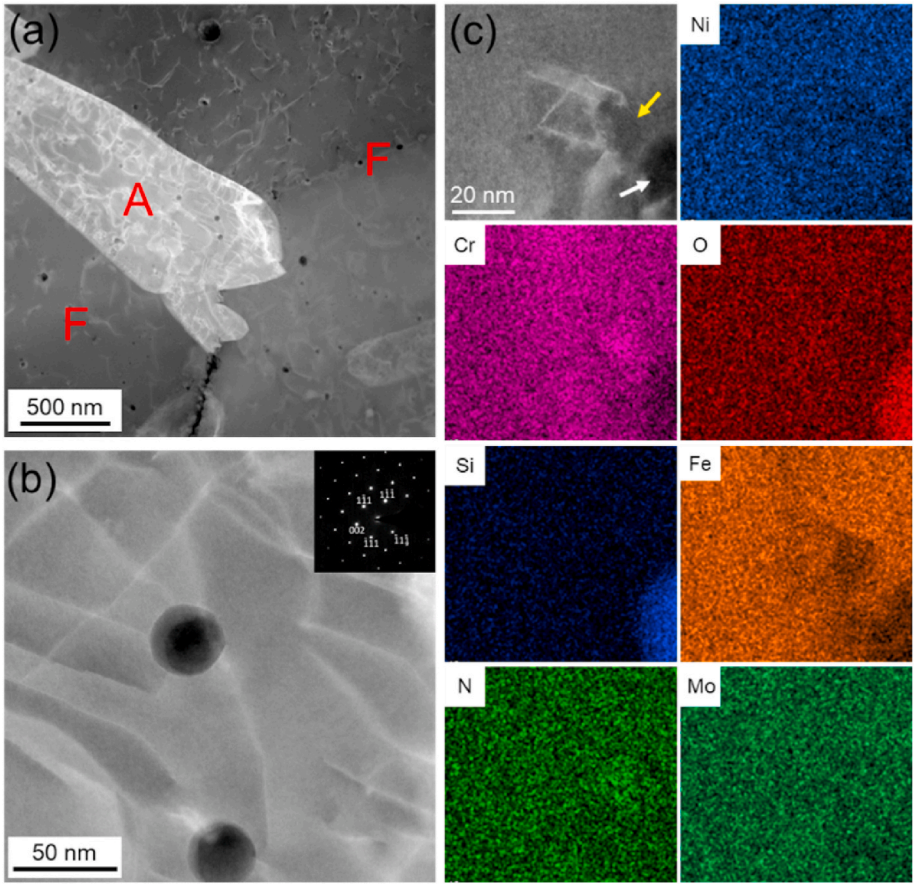

Fig. 5. (a,b) Low angle annular dark field (LAADF) STEM images of typical grain morphologies, dislocations and stacking faults within the austenite phase (inset in (b) showing SAD pattern of the austenite phase). (c) TEM and corresponding elemental map of segregation in different phases. Silicon oxide and Cr_2N particles are marked by white and yellow arrows in (c), respectively. A and F in (a) refer to austenite and ferrite, respectively.

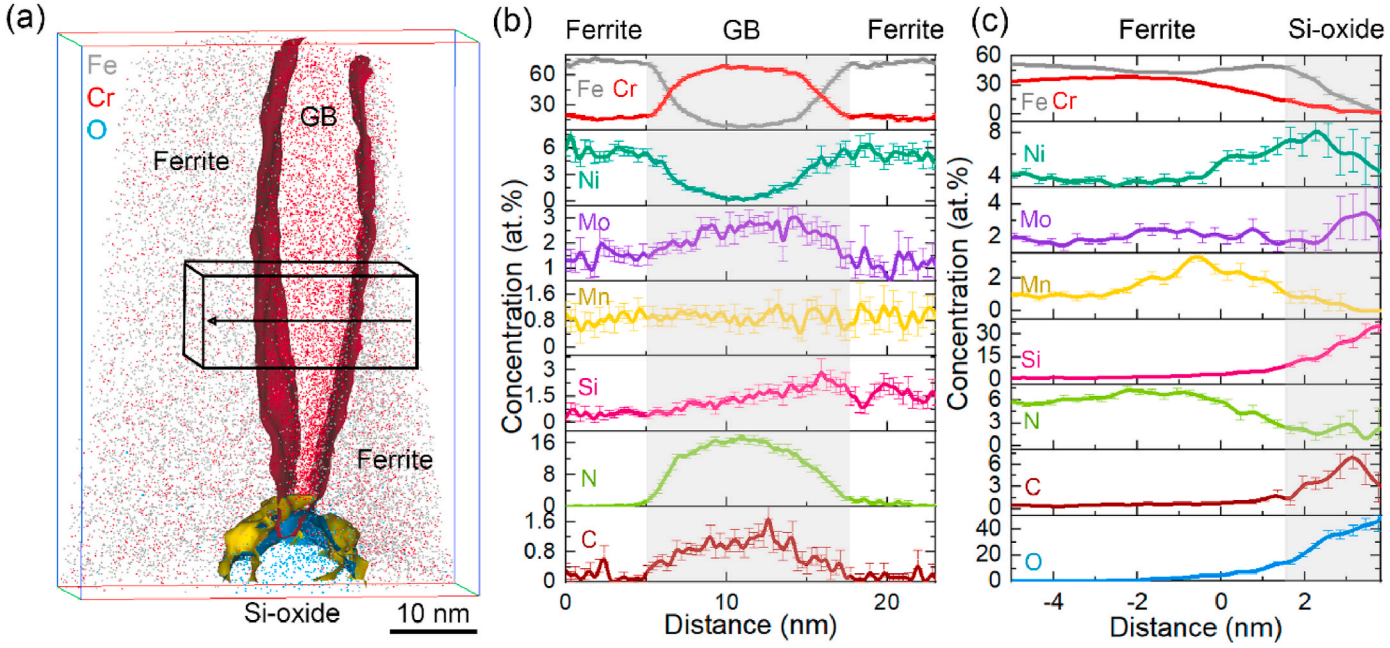

Fig. 6. (a) 3D atom distribution maps of Fe, Cr, and O across the grain boundary. 48.0 at.% Cr, 5.0 at.% O, and 2.0 at.% Mn iso-concentration surfaces are shown in red, blue, and yellow, respectively. (b) 1D concentration profiles of the black box across the grain boundary shown in (a). (c) Proxigram based on 5.0 at% O iso-concentration surfaces.

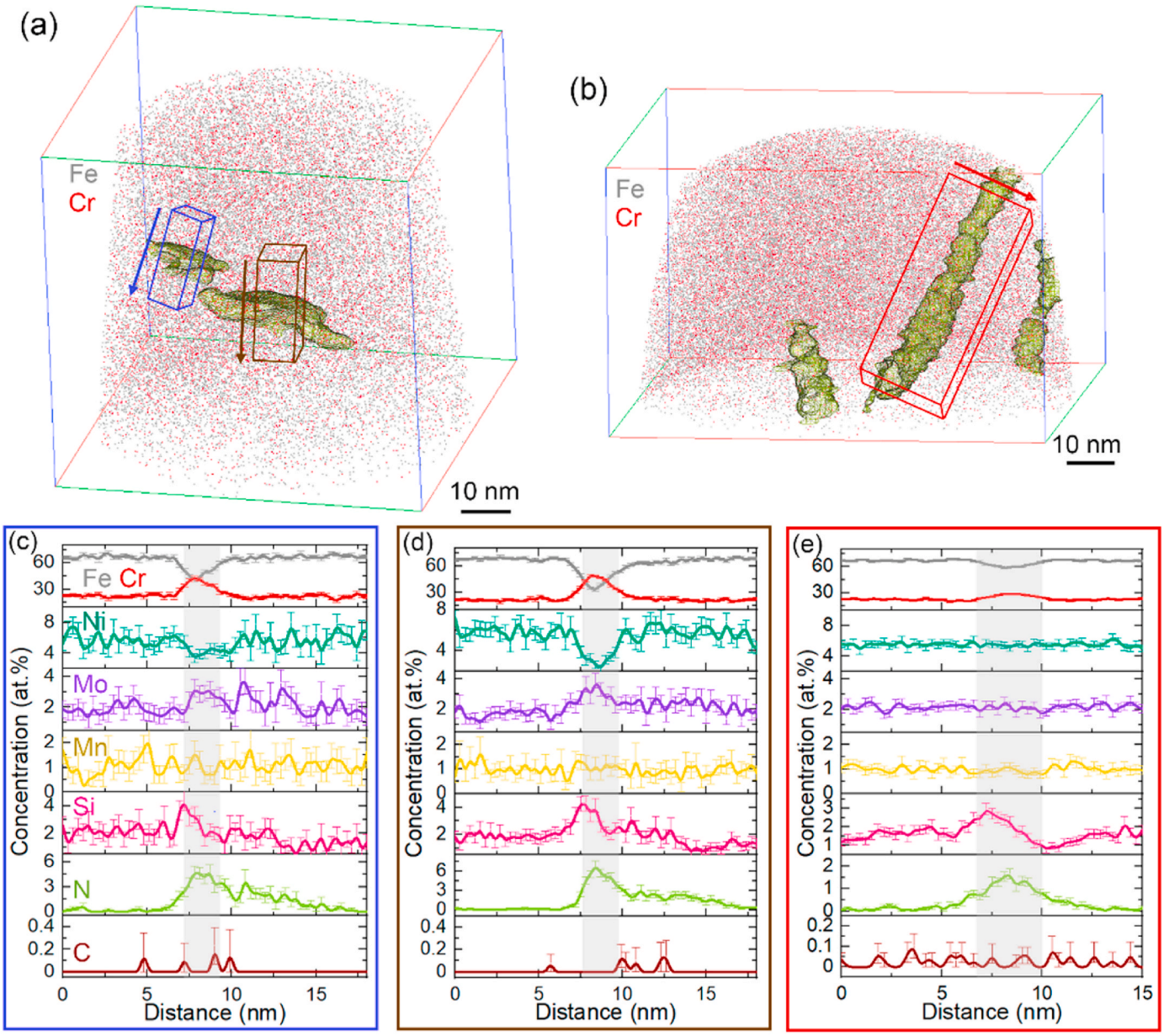

Fig. 7. (a) 3D atom distribution maps of Fe, Cr and 2.5 at.% N iso-concentration surfaces showing plate-like Cr_2N particles. (b) 3D atom distribution maps of Fe, Cr and 0.5 at.% N iso-concentration surfaces showing rod-like Cr_2N particles. (c) 1D concentration profiles of the blue box in (a). (d) 1D concentration profiles of the brown box in (a). (e) 1D concentration profiles of the red box in (b).

Impact toughness values of the samples in both LPBF and LPBF + HT conditions show strong dependence on the microstructure, loading direction and temperature (Fig. 12). Due to the typical microstructural anisotropy resulted from LPBF, samples printed in two different orientations are studied in detail here. Samples with V-notches perpendicular to the build direction show almost similar low impact toughness values of 6 ± 1 J/cm^2 at room temperature and 5 ± 1 J/cm^2 at −110 °C. Samples with AM build direction parallel to the V-notch show similarly low impact toughness values of 5 ± 1 J/cm^2 at −110 °C. This material condition, however, offers an acceptable toughness level (59 ± 4 J/cm^2) at room temperature. Heat treatment at 1000 °C results in a significant increase in toughness. Irrespective of the orientation of the notch with regards to the build direction, the LPBF + HT materials show an impact toughness of ~120–130 J/cm^2 at room temperature (130 ± 9 J/cm^2 for HT perpendicular, 121 ± 18 for HT parallel). Interestingly, the LPBF + HT samples with V-notch perpendicular to the build direction exhibit almost the same impact toughness at −110 °C (126 ± 31 J/cm^2). The LPBF + HT samples with V-notch parallel to the build direction show comparatively lower toughness (52 ± 9 J/cm^2) at −110 °C, although still above 40 J/cm^2, which is usually considered as a threshold for the ductile to brittle transition [19].

Fracture surfaces of individual Charpy samples show distinct features in line with the impact energy trends. The surface of samples with high impact toughness (e.g., LPBF + HT samples with V-notch parallel or perpendicular to the BD) show a ductile failure, dominated by dimple-dominant rupture both at RT and at −110 °C (Fig. 12c,d,e, and g). In the sample with average toughness (i.e., LPBF sample at RT with notch parallel to BD), the splits and the main cracks appear to propagate along ferrite-ferrite grain boundaries (Fig. 12d). Small local regions with cleavage fractures can also be detected (Fig. 12d). By contrast, fracture surfaces of the samples with low impact toughness (e.g., LPBF samples with BD perpendicular to notch when tested at RT and −110 °C, and LPBF samples with BD parallel to notch when tested at −110 °C) reveal a brittle fracture surface dominated by cleavage facets (Fig. 12b,f). In

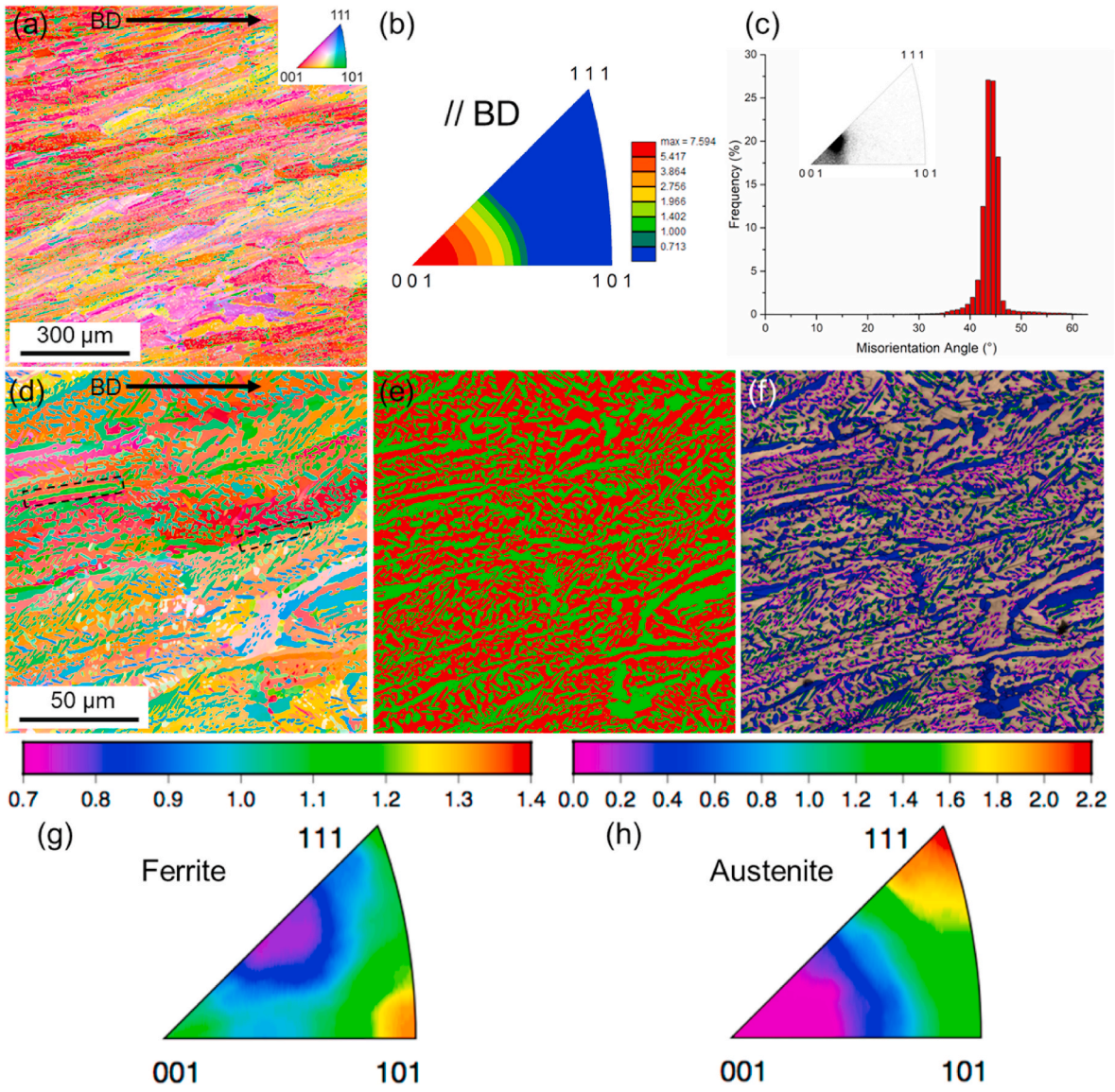

Fig. 8. (a) EBSD IPF map (along the build direction) taken from the central region of the DSS builds processed by LPBF and subjected to heat treatment. (b) Texture (IPF) of ferrite along the BD. (c) Misorientation angle between austenite and ferrite with the inset showing the misorientation axis at the angle of 42–46°. (d) Higher magnification IPF map of the same region in (a) with black dashed rectangles pointing out examples of allotriomorph austenite. (e) phase map corresponding to (d) with ferrite coloured red and austenite coloured green. (f) Image quality map of the region in (d) and (e) with austenite coloured blue. Magenta lines refer to KS and green lines refer to NW interfaces between austenite and ferrite. (g, h) Grain boundary habit plane distributions for ferrite and austenite, respectively, for all austenite-ferrite boundaries irrespective of misorientation. 48,914 austenite/ferrite boundary segments were used to plot these heat maps. The colour keys show MRD.

these cases, the ferrite matrix is of a glossy bright surface with a straight fracture path. Some small dimples are also observed locally, presumably indicating the ductile fracture within austenite (see Fig. 12b). Another feature of the fracture surfaces is the high fraction of voids in ductile samples compared to a mostly cleavage appearance with minimum voids in the low toughness samples (compare Fig. 12g,c to 12b). To clarify the deformation mechanism of the samples that show outstanding toughness at −110 °C (e.g., LPBF + HT sample with notch parallel to the BD) their microstructure in regions close to the fracture surface was examined in detail (Fig. 13). A site-specific TEM study of a lamella at the regions very close to the fracture surface clearly confirms the occurrence of twinning within austenite while no twinning is observed within ferrite.

4. Discussion

The current study provides new insights into the phase transformation from ferrite to austenite in DSS during LPBF and upon post heat treatment. It is shown that the unique nature of solidification and phase transformation during LPBF affects the character of interfaces between austenite and ferrite both in the as-built condition and after the subsequent heat treatment. Such significant differences in the microstructure evolution of additively manufactured DSS compared to conventional DSS can result in mechanical properties different to wrought counterparts as discussed below.

4.1. Evolution of ferrite during LPBF and heat treatment

The microstructure of 2205 DSS in the LPBF condition is mostly ferritic in line with previous reports [11]. The columnar ferrite grains

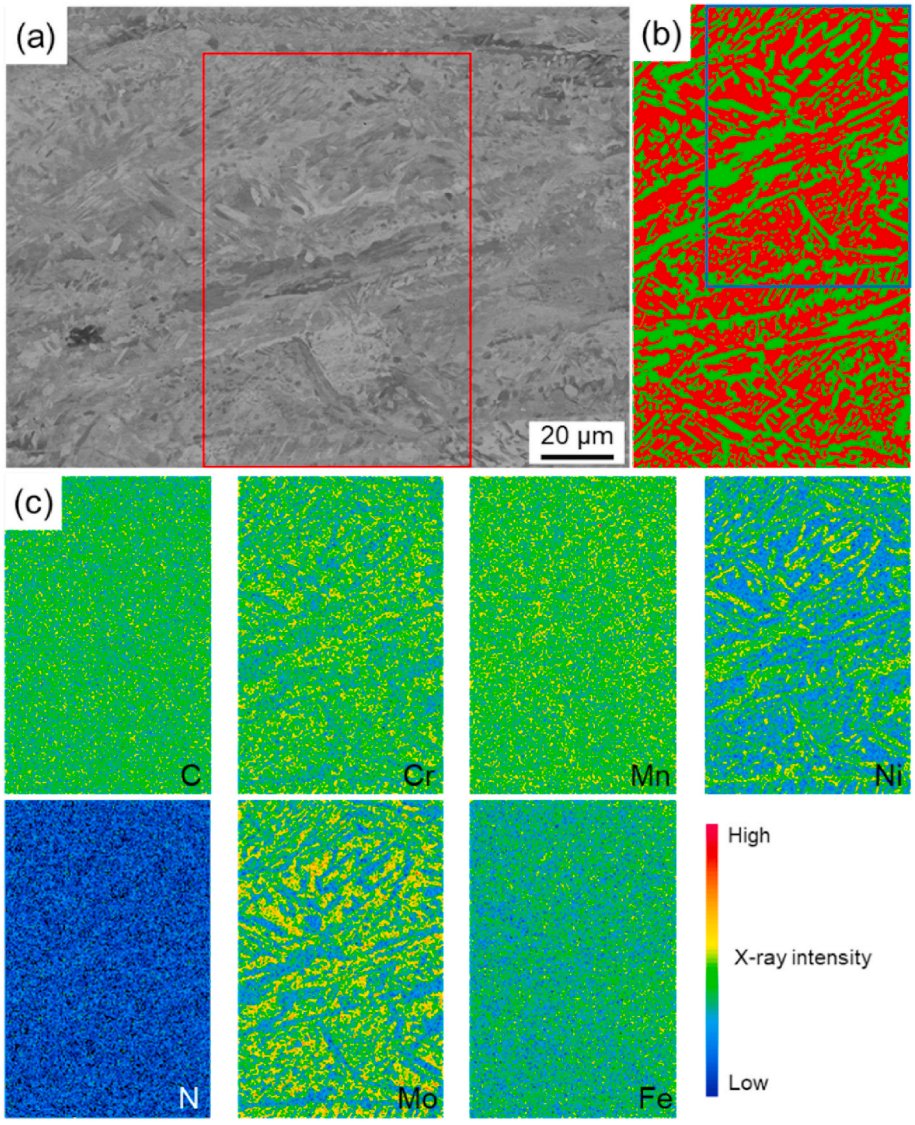

Fig. 9. (a) SEM image of the LPBF and heat treated DSS, the blue square indicates the area of the EPMA map, b) EBSD phase map of the same region with ferrite in red and austenite in green. The blue square indicates the area of the EPMA map. (c) EMPA elemental maps of C, Cr, Mn, Ni, N, Mo, and Fe.

are elongated along the build direction and have a strong <100> texture. This is related to directional solidification along the build direction and <100> being the preferred solidification direction with the highest heat flow for the ferrite grains [31]. Such alignment of the build and growth directions results in an epitaxial growth across several layers.

Two factors of rapid cooling, that results in austenite bypassing, and the loss of N during melting, can result in excessive ferritisation during AM of DSS [11,32]. N has been shown to promote austenite formation during the ferrite to austenite transformation on cooling by increasing both the start and finish temperatures of the phase transformation [33]. Multi-pass welding of DSS has already been shown to cause N loss during multiple re-melting steps [34]. Without N being introduced into the chamber during printing, N escapes from the melt pool to increase the N content in the environment [35]. It is to be noted that while N loss has been reported in arc-based welding and arc-based AM processes, these processes have large melt pools and remains liquid for longer periods compared to the LPBF process. Analysis of the LPBF DSS and PH stainless steels [12,36,37] for example shows no significant N loss. These reports together with the fact that a short heat treatment can recover the austenite content (see Fig. 8), implies that the effect of N loss is not significant compared to that of the thermal profile in the low austenite volume fraction in our study.

The fast cooling associated with LPBF generates a supersaturation of N inside ferrite that results in a large density of Cr_2N. Karlsson and Arcini [38] reported the preferential formation of nitrides within ferrite in DSS welds. This can be related to relatively higher diffusion rates of elements in ferrite compared to austenite and low solubility of interstitials in body centred cubic (BCC) crystal structures. In the welding literature, Ni-enriched filler metals, N shielding, and control of the heat input have been suggested to supress the formation of nitrides and result in a balance in ferrite-austenite volume fraction [39]. Interestingly, it has been shown that single or double melting does not lead to extensive nitride formation, but intergranular nitrides form after remelting for three or four times [32]. Intergranular nitrides are therefore termed 'isothermal nitrides' suggesting that they are presumably formed during sequential melting and solidifying of overlaying powders on top of an already solidified layer. This is opposed to intragranular Cr_2N particles that are formed directly from the melt-pool which are often called 'quenched-in' nitrides [40]. The LPBF DSSs show both of these Cr_2N types (see Figs. 4–7).

Despite the high volume fraction of Cr_2N, no σ or carbide phases are detected in the LPBF sample. It has been reported that with increasing N content, the expected fraction of Cr_2N increases [41]. However,

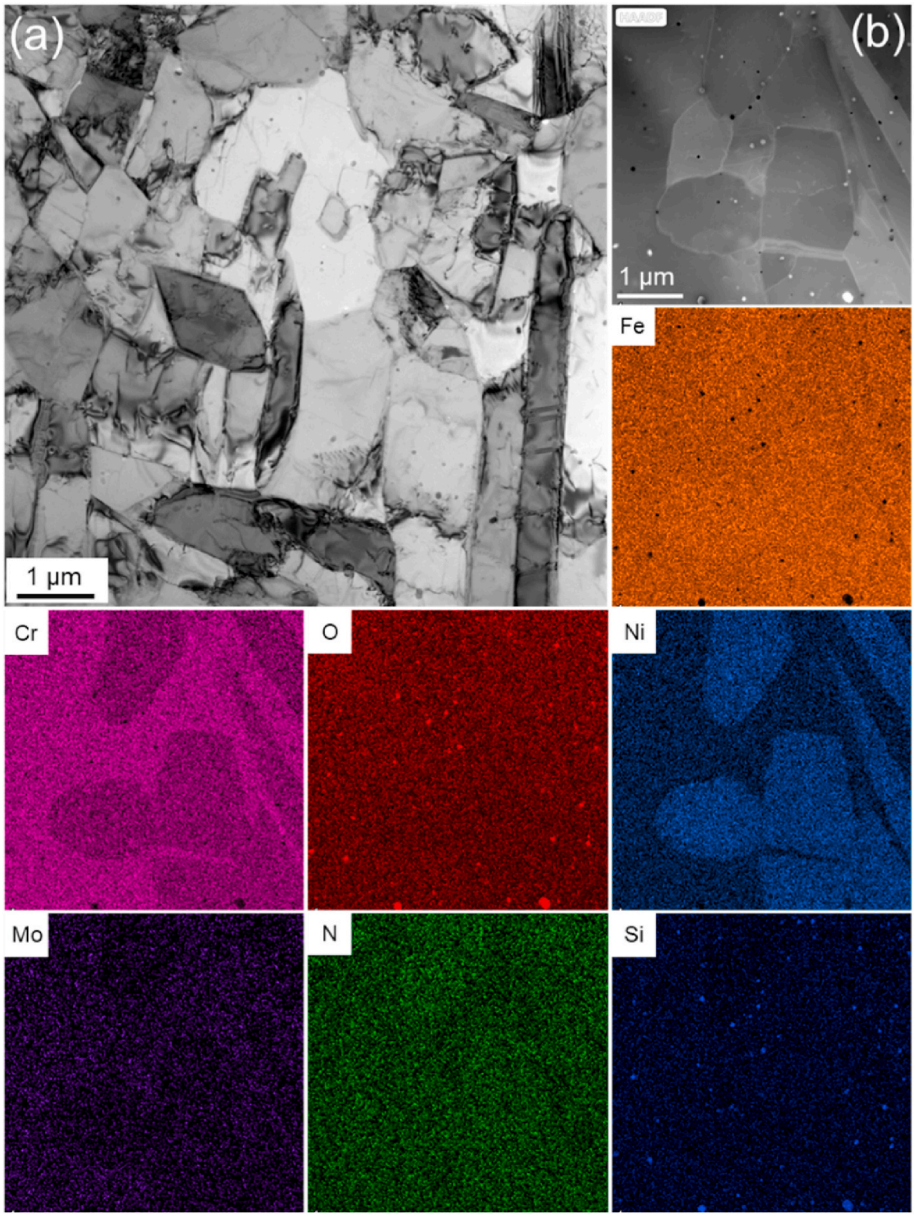

Fig. 10. (a) Bright field TEM images showing grain morphology and defects in the sample after LPBF and heat treatment (LPBF + HT). (b) HAADF and corresponding elemental distribution maps showing partitioning of alloying elements between ferrite and austenite.

according to Zubchenko [42], N lengthens the incubation period for σ phase nucleation. N also lowers the diffusion rate of Cr and Mo (the main constituents of σ), which in turn makes it difficult to achieve the concentration required for σ to form [41]. The reason why carbides do not form is suggested to be related to the fact that the chemical potential gradient driving N into ferrite is higher than that of C, which saturates N in ferrite matrix [43], leading to subsequent nitride formation. C, however, can usually be accommodated via segregation to dislocation cores and low-angle grain boundaries [44]. Kinetics effects can be considered as another factor for the absence of σ and carbides. For example, using computational modelling of LPBF, Mukherjee et al. [45], have predicted the time and temperature profile of a 316L during LPBF process. Their results show that even the reheating from subsequent passes and layers may not provide the time and temperatures required to form these phases.

The LPBF microstructure also contains a high density of dislocations due to the severe thermal contraction stresses induced by rapid solidification. These dislocations are mostly annihilated upon annealing (see Fig. 10). Ferrite retains its <100> texture during the heat treatment (see Fig. 8b) indicating it does not recrystallize. During annealing, ferrite experiences static recovery dominated by dislocations annihilation. This is different to recovery via polygonisation where dislocations arrange themselves into cell boundaries [21].

4.2. Ferrite to austenite phase transformation

Upon heat treatment, austenite particles nucleate and grow rapidly in high numbers as the LPBF material with the ferritic microstructure has a super-saturation of austenite forming elements. Intragranular austenite particles emerge within the ferrite matrix with some of them nucleating and growing along sub-grain (cell) boundaries [11]. Another contributing factor to the high density of austenite nuclei is the presence of sub-micron silicon oxide resulting from LPBF [46]. Furthermore, the dislocations induced by LPBF can also act as nucleation sites for austenite. Dislocations result in high free energy that increases the diffusion rate of elements and as such contributes to the nucleation and

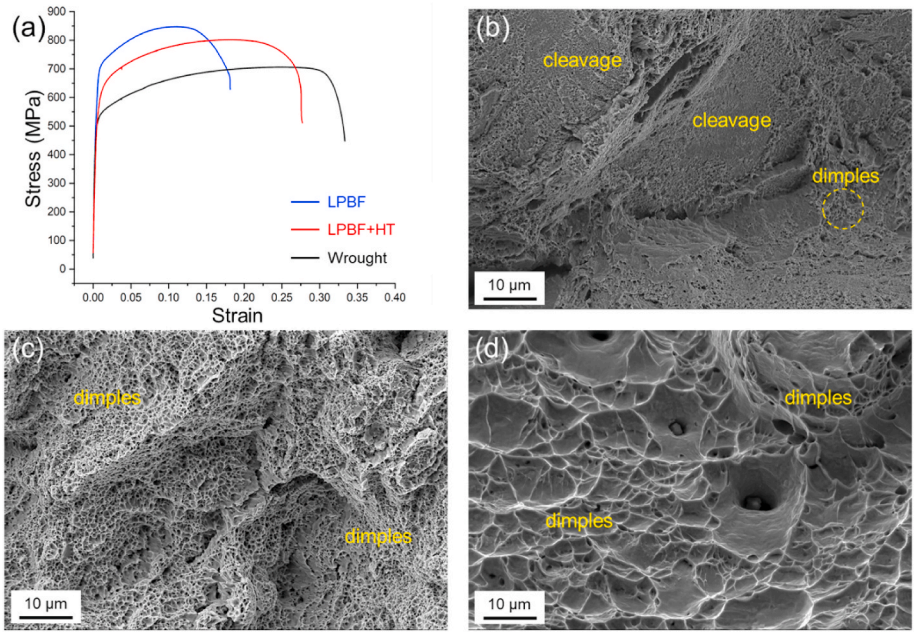

Fig. 11. (a) Representative tensile stress-strain curves of the DSS samples in as-printed (LPBF) and after heat treatment (LPBF + HT) conditions benchmarked against a wrought DSS sample. (b, c, d) Post-tensile testing SEM micrographs of fracture surfaces of the LPBF sample, LPBF + HT sample, and wrought samples, respectively.

growth of austenite. Such abundance of nucleation sites for austenite minimises the distance between nuclei, facilitates the diffusion of supersaturated N, and results in significant refinement of austenite particles.

Formation of austenite can occur on existing Cr_2N particles. One can hypothesise that the depletion of Cr in the regions adjacent to a Cr_2N particle will provide suitable sites for nucleation of austenite. However, it has been previously shown that if N is also depleted in the these regions, the driving force for the austenite formation will be reduced rather than increased [17]. The APT analysis in the current work implies that there is no significant depletion of these elements adjacent to the Cr_2N particles (see Figs. 6 and 7). Thus, the main driving force for austenite to form on Cr_2N particles would be the classical minimisation of the interfacial energy through nucleation on existing interfaces and formation of low-energy interfaces between $(0001)_{Cr2N}$ and $(111)_{\gamma}$ as denoted by Ramirez et al. [46]. Post-mortem observation of nucleation of austenite on nitrides is challenging as the trapped intragranular nitrides inside the austenite would promptly be dissolved [47]. During annealing, austenite particles grow to a certain extent. They do not substantially coarsen further due to the soft impingement phenomena (diffusion field overlap of neighbouring grains) which decelerates the overall phase transformation kinetics [48].

The ferrite to austenite phase transformation mechanism during LPBF of DSS is complex. As this transformation occurs under high undercooling and, therefore, at low temperatures, diffusional partitioning only occurs for interstitials (i.e., C and N) taking the material into a para-equilibrium state. However, once the lattice change occurs, elastic strains will be created which, if not relaxed, will hinder a further progression of the phase transformation. These strains can be relaxed via diffusion in reconstructive transformations at elevated temperatures [3]. However, alternative mechanisms need to be involved to relax them at the high cooling rates associated with LPBF. It is hypothesised that a "shear assisted diffusional" mechanism can potentially explain the formation and chemistry of austenite [17]. In this model, the phase change is assumed to occur through interstitial atoms diffusing, as occurs in diffusional transformations. The elastic strains are, however, relaxed through a lattice invariant shear by slip displacements.

Upon annealing at 1000 °C, the interfaces between austenite and ferrite are largely coherent (Fig. 8) which is usually a feature of a displacive phase transformation [3]. At the same time, there is a considerable partitioning of alloying elements (Figs. 9 and 10) which shows that at least the growth of austenite must have occurred in a diffusional manner. Interestingly, there is a significant tendency towards the KS orientation relationship (OR) compared to NW OR during the growth of austenite (Fig. 8f). This can be related to a number of reasons including the facts that the KS OR allows the optimum deviation between stepped interface planes with the close-packed planes [49], and the KS OR minimises the coherent elastic energy of the austenite-ferrite interfaces [50]. Another factor worth mentioning is the traces of C and S existing in the initial powders, which have been reported to shift the austenite/ferrite OR from NW to KS in DSSs [51].

The termination of ferrite on {100} in the LPBF sample (Fig. 2g) is an interesting and unexpected observation. Previous reports have shown that in ferrite, {111} surfaces are expected to exhibit the minimum energy at low temperatures [52]. Also, considering the BCC structure of ferrite, {110} is expected to be the most densly close-packed plane. The termination of ferrite on {100} planes, therefore, contrasts with both crystallographic and energy minimisation criteria. We believe that the termination of ferrite at {100} in the current work is related to the ferrite texture and the geometry of austenite. Firstly, the strong <100> ferrite texture means grains are aligned so that [001] is parallel to the BD. This will enforce plane normals to be perpendicular to [001], i.e., they will need to be of a [hk0] normal direction. While this can explain why {111} is not seen, this condition alone is not enough to create a preference for {100} planes over other {hk0} planes. However, our EBSD analysis shows that there is a special geometry to austenite formed at ferrite-ferrite boundaries. As seen in Fig. 2e, austenite forms in an allotriomorphic morphology and the austenite-ferrite boundaries appear to be often perpendicular or parallel to BD. This means that the boundary perpendicular to the image plane (which is the stereologically most probable plane) is always a {100} type, and this leads to the increase of the population at {100}. Therefore, the directional solidification of ferrite along <100> during AM, together with the preponderance of austenite-ferrite boundaries situated perpendicular and parallel to this direction makes ferrite grains to preferably terminate on {100} habit planes. Upon subsequent growth of austenite inside ferrite grains, austenite and ferrite will have the opportunity to adjust their geometry and habit planes in such a way that the interface energy is minimized.

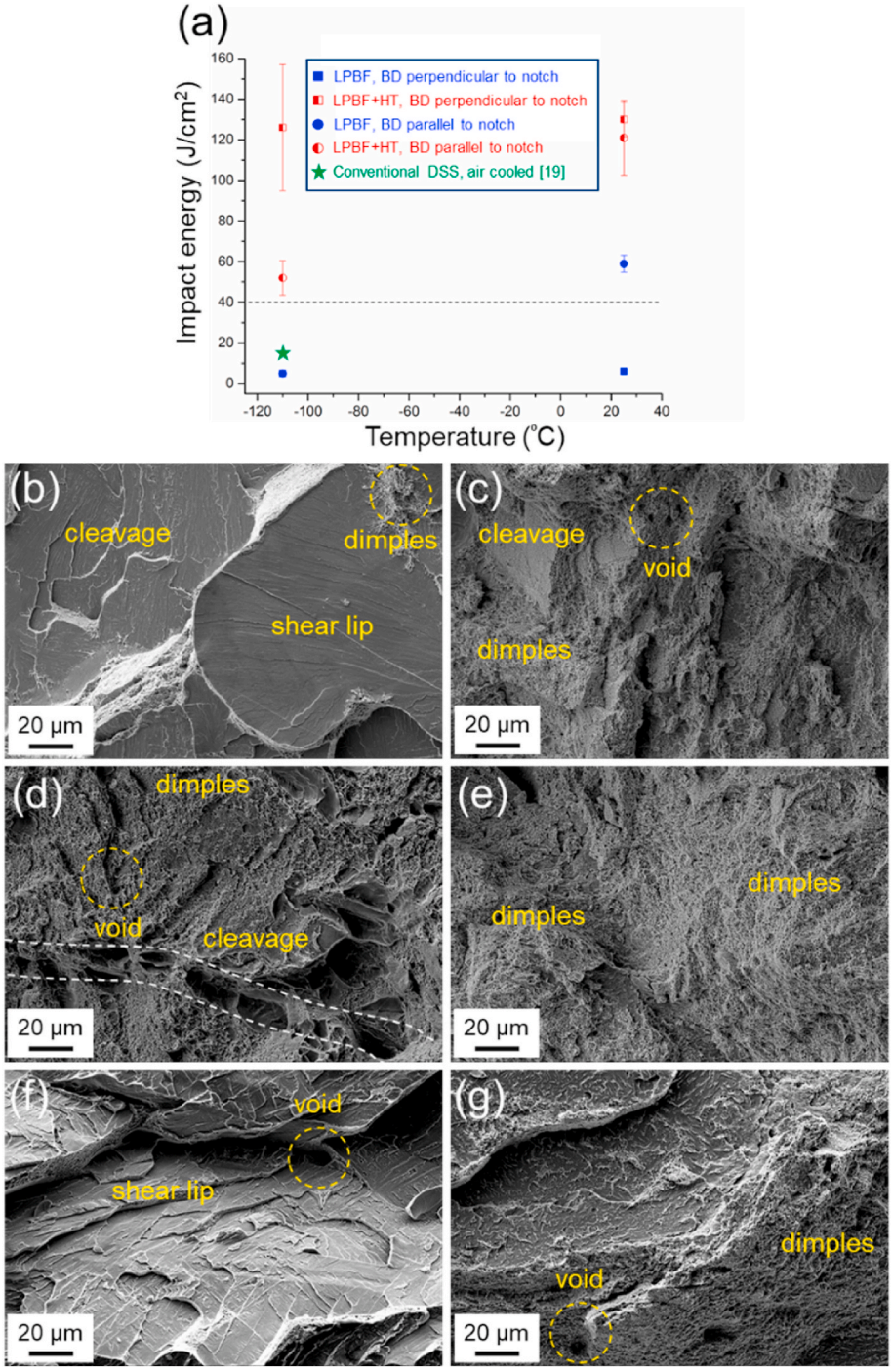

Fig. 12. (a) Impact toughness energy values for different microstructures at different temperatures of RT and −110 °C in two different directions of notches, parallel and perpendicular to BD. The toughness values at −110 °C are compared to conventionally processed DSS from Ref. [19]. The dashed line shows the 40 J/cm^2 threshold for ductile to brittle transition. (b–g) Post-fracture SEM images of the fracture surfaces of Charpy samples for different initial microstructures tested in different directions and at different temperatures; (b) LPBF sample at room temperature (RT) with notch perpendicular to BD, (c) LPBF + HT sample with a notch perpendicular to BD, (d) LPBF sample at RT with notch parallel to BD, (e) LPBF + HT sample with notch parallel to BD. (f) LPBF sample at −110 °C with notch parallel to BD. (g) LPBF + HT sample at −110 °C with notch parallel to BD. The white dashed region in (d) is believed to represent a grain boundary.

This will result in the dominance of $\{110\}_F//\{111\}_A$ interfaces (see Fig. 8 g, h).

4.3. Evolution of mechanical properties

As-printed (LPBF) DSS shows an exceptionally high strength that can be related to a number of microstructural features. Firstly, the microstructure is mostly ferritic, and it is generally known that ferrite is the hard phase within DSS. This is exacerbated in the case of LPBF DSS due to the high supersaturation of alloying elements in ferrite. Precipitation hardening by ultra-fine Cr_2N particles is another contributing factor (Figs. 4–7). Further, due to the residual stresses induced by the thermal gradients of LPBF, a high dislocation density is observed in the as-built material (see Figs. 4 and 5) making it difficult to plastically deform. While these factors all contribute to a higher YS and UTS, they cause a drop in the ductility of the material compared to the conventionally manufactured DSS. Heat treatment of LPBF samples recovers the ductility to an acceptable level while additionally offering higher YS and UTS compared to conventional DSS.

The improvement in ductility after heat treatment is mostly related to the increase in the austenite fraction from ~2% to ~45% (compare Figs. 8 and 2). It is known that a severe load partitioning occurs in DSS during deformation and the initial stages of plastic deformation is accommodated by the softer austenite phase [19]. Considering the higher ductility of austenite compared to ferrite, increasing austenite fraction will in general improve the ductility. This is important in the

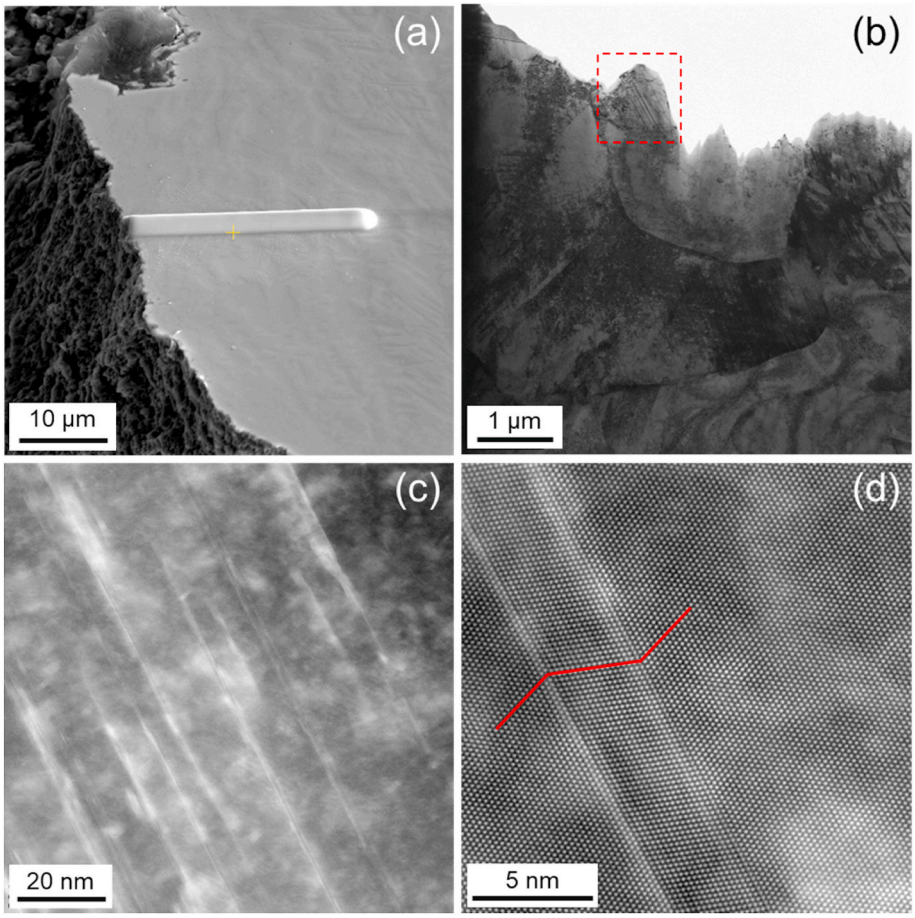

Fig. 13. (a) SEM image of the fracture surfaces of LPBF + HT sample after Charpy test at −110 °C with notch parallel to the BD. The region of interest where the foil were extracted from has been ion beam deposited for protecting. (b) Bright field TEM image showing the grain morphology and twinning in the deformed sample. (c, d) High-resolution LAADF-STEM images showing twinning in a $<110>_{FCC}$ austenite grain. (c) and (d) are higher magnification images of the area dashed in (b).

LPBF material in comparison to the wrought material as austenite particles are very fine in the LPBF material (i.e., ~2 μm diameter) compared to typical austenite grain size in wrought samples (~30–50 μm). At a certain level of straining, however, strain will be transferred into ferrite. This mostly occurs through the high population of coherent austenite-ferrite interfaces that facilitate slip transition at interphase boundaries. The coherence of the interfaces (see Fig. 8) hinders the accumulation of stresses, avoiding interfacial cracking [53], hence, contributing to high ductility. The dissolution of Cr_2N and annihilation of dislocations within ferrite during the heat treatment are the other factors contributing to the improvement of ductility. Finally, the dispersed spatial distribution of austenite particles within ferrite can blunt cracks developed within ferrite and in turn increase the ductility. These observations are manifested in the fracture surfaces of samples revealing a mixed brittle-ductile fracture in the LPBF sample, compared to a ductile dimple-dominant fracture in the heat-treated (LPBF + HT) condition (see Fig. 11).

The impact toughness of LPBF DSS is affected by macro, micro and nano-scale features. Firstly, on a macro-scale, the sharp difference between the toughness of LPBF material in different directions can be explained through the layer-wise nature of deposition during LPBF. The potential discontinuity at the interface between individually deposited layers can act as a preferred path for crack growth [54]. This is seen in our study where loading is perpendicular to the building direction. If loading is parallel to the building direction, the interlayer boundaries may cause the cracks to branch and relax the tri-axial tensile stresses near crack tips, deflect the crack path, and supress the crack propagation [19]. Irrespective of the building direction, the LPBF material shows low impact toughness at −110 °C. This is rationalized considering the high tendency of ferrite (in contrast to austenite) to experience ductile-to-brittle transition at low temperatures [55].

After the heat treatment, a comparatively high impact toughness at both RT and −110 °C is achieved, although the reason behind the comparatively lower toughness of the LPBF + HT samples with V-notch parallel to the BD compared to its 'perpendicular to BD' counterpart remain unknown and requires further in-depth studies. Generally, the heat treatment maximises the volume fraction of austenite and dissolves the brittle Cr_2N particles (see Figs. 8 and 10). The abundance of austenite particles homogeneously distributed within ferrite matrix blunts and deflects cracks initiated in the ferrite. In addition to these geometrical considerations, the termination of ferrite grains at {110} planes at the ferrite-austenite interfaces after the heat treatment can contribute to the improvement in toughness. The {110} habit plane is expected to increase the plasticity and enhance the impact toughness [56]. It is to be noted though that there are still controversies over this mechanism with some researchers reporting {100} planes of ferrite to have the highest contribution to impact toughness [57]. However, the current results clearly give strength to the idea of $\{110\}_F$ planes being the preferred planes for increased plasticity and therefore highest toughness and tensile ductility.

Another critical factor determining the impact toughness of duplex stainless steels is the ferrite grain size, with the ductile-to-brittle transition temperature (DBTT) being expected to decrease with grain refinement [19]. While the apparent ferrite grain size (~110 μm) did not change significantly during the heat treatment, the effective grain size of ferrite where cracks can grow freely was substantially decreased with

the introduction of austenite (compare Figs. 2 and 8). Lower effective ferrite grain sizes can also supress mechanical twinning [19]. It is generally accepted that deformation twinning within ferrite can substantially deteriorate the toughness [19], while deformation twining within austenite is beneficial for toughness [58]. Previous studies have shown that in a DSS air-cooled from the fully ferritic region, ferrite goes through deformation twinning during impact testing at −110 °C [19]. The site-specific TEM study of the regions close to the fracture surface in the current work clearly shows the occurrence of twinning within austenite during impact loading while no twinning is observed within ferrite (see Fig. 13). This again indicates the preferential partitioning of load towards the austenite. Austenite has a relatively low stacking fault energy (SFE) which makes it prone to the formation of stacking faults that would act as nucleation sites for deformation twinning during impact loading. The resistance of ferrite against deformation twinning and the propensity of austenite for deformation twinning in the LPBF + HT sample, therefore, is another reason behind the recovery of impact toughness after heat treatment.

5. Conclusions

New insights into the evolution of microstructure and mechanical properties during LPBF and post-LPBF heat treatment of 2205 duplex stainless steel are provided. Particular attention is laid on advancing the understanding of the phase transformation mechanism and the evolution of the interphase boundary character distribution during both LPBF and post-LPBF heat treatment. Different microstructural features significantly affect the mechanical properties of LPBF DSS, with opportunities available to tune the microstructure via LPBF and heat treatment to achieve mechanical properties comparable to those in traditionally manufactured DSS. The main conclusions are:

1 The microstructure of 2205 DSS in the as-built (LPBF) condition is mostly ferritic. This is related to the extremely fast cooling rate during LPBF. Small fractions of austenite are mostly formed at the ferrite-ferrite grain boundaries via a phase transformation accompanied with diffusion of interstitial C and N atoms.
2 Austenite/ferrite interfaces are shown to terminate on $\{100\}_F//\{111\}_A$ in the LPBF condition, which contrasts the energetically and crystallographically preferred habit plane by ferrite. The directional solidification of ferrite along <100> during LPBF, together with the preponderance of austenite-ferrite boundaries situated perpendicular and parallel to this direction makes ferrite grains to terminate on {100} habit planes.
3 Upon a short heat treatment at 1000 °C, the microstructure can be reverted into its equilibrium in terms of phase balance (~45% austenite). The new interfaces created upon intragranular nucleation and growth of intergranular/intragranular austenite terminate on crystallographically and energetically favoured $\{111\}_A//\{110\}_F$ habit planes.
4 The LPBF sample shows a high strength (UTS = 844 MPa) but low ductility (El = 18%) due to its mostly ferritic structure, an abundance of Cr_2N particles, and a high density of dislocations. These microstructural features also result in a low impact toughness.
5 Upon heat treatment at 1000 °C, the ductility of the steel is substantially improved, while YS and UTS (563 and 798 MPa, respectively) are still higher than in a wrought alloy (493 and 709 MPa, respectively), implying the possibility of achieving an optimum combination of tensile properties via LPBF followed by heat treatment (HT).
6 LPBF + HT DSS steel shows acceptable impact toughness at −110 °C compared to its conventional counterpart in the air-cooled condition. This is related to the fine austenite particles evenly distributed within ferrite that blunt cracks and accommodate the plastic deformation via twinning and refrain ferrite from mechanical twinning.

Data availability statement

The raw/processed data required to reproduce these findings cannot be shared at this time as the data also forms part of an ongoing study.

CRediT authorship contribution statement

Nima Haghdadi: Methodology, Conceptualization, Formal analysis, Investigation, Data curation, Writing – original draft, Writing – review & editing. **Carina Ledermueller:** Formal analysis, Data curation, Writing – review & editing. **Hansheng Chen:** Formal analysis, Data curation, Writing – review & editing. **Zibin Chen:** Formal analysis, Data curation, Writing – review & editing. **Qian Liu:** Methodology, Formal analysis, Writing – review & editing. **Xiaopeng Li:** Methodology, Conceptualization, Writing – review & editing. **Gregory Rohrer:** Methodology, Conceptualization, Writing – review & editing. **Xiaozhou Liao:** Conceptualization, Writing – review & editing, Funding acquisition. **Simon Ringer:** Conceptualization, Writing – review & editing, Funding acquisition. **Sophie Primig:** Methodology, Conceptualization, Writing – review & editing, Funding acquisition, Supervision.

Declaration of competing interest

The authors declare that they have no known competing financial interests or personal relationships that could have appeared to influence the work reported in this paper.

Acknowledgements

Funding from the AUSMURI program administered by the Australia's Department of Industry, Science, Energy and Resources is acknowledged. The authors acknowledge the facilities, as well as the scientific and technical staff support of the Electron Microscope Unit (EMU) at UNSW Sydney (part of the Mark Wainwright Centre) and Sydney Microscopy & Microanalysis (SMM) at the University of Sydney (a core research facility). Both the EMU and SMM are nodes of Microscopy Australia. Support from Drs Vijay Bhatia, Magnus Garbrecht, Hongwei Liu and Takanori Sato (SMM) are particularly acknowledged. N. Haghdadi thanks Dr. Majid Laleh at Deakin University for fruitful discussions. S. Primig is supported under the Australian Research Council's DECRA (project number DE180100440) and the UNSW Scientia Fellowship schemes.X. Li would like to acknowledge the financial support from Australian Research Council (ARC) Discovery Early Career Researcher Award (DECRA) DE190101495.

Appendix A. Supplementary data

Supplementary data to this article can be found online at https://doi.org/10.1016/j.msea.2022.142695.

References

[1] R.N. Gunn, Duplex Stainless Steels: Microstructure, Properties and Applications, Woodhead Publishing, Cambridge, 1997.
[2] M. Pan, X. Zhang, P. Chen, X. Su, R.D.K. Misra, The effect of chemical composition and annealing condition on the microstructure and tensile properties of a resource-saving duplex stainless steel, Mater. Sci. Eng. 788 (2020) 139540.
[3] N. Haghdadi, P. Cizek, P.D. Hodgson, V. Tari, G.S. Rohrer, H. Beladi, Effect of ferrite-to-austenite phase transformation path on the interface crystallographic character distributions in a duplex stainless steel, Acta Mater. 145 (2018) 196–209.
[4] G.C.L.D. Freitas, G.S. da Fonseca, L.P. Moreira, D.N.F. Leite, Phase transformations of the duplex stainless steel UNS S31803 under non-isothermal conditions, J. Mater. Res. Technol. 11 (2021) 1847–1851.
[5] J. Johansson, M. Odén, X.H. Zeng, Evolution of the residual stress state in a duplex stainless steel during loading, Acta Mater. 47 (2009) 2669–2684.
[6] M. Roudnická, O. Molnárová, J. Drahokoupil, J. Kubásek, J. Bigas, V. Šreibr, D. Paloušek, D. Vojtěch, Microstructural instability of L-PBF Co28Cr6Mo alloy at elevated temperatures, Addit Manuf 44 (2021) 102025.

[7] Y. Kok, X.P. Tan, P. Wang, M.L.S. Nai, N.H. Loh, E. Liu, S.B. Tor, Anisotropy and heterogeneity of microstructure and mechanical properties in metal additive manufacturing: a critical review, Mater. Des. 139 (2018) 565–586.

[8] R. DeMott, N. Haghdadi, Z. Gandomkar, X. Liao, S. Ringer, S. Primig, Formation and 3D morphology of interconnected α microstructures in additively manufactured Ti-6Al-4V, Materialia 20 (2021) 101201.

[9] N. Haghdadi, M. Laleh, M. Moyle, S. Primig, Additive manufacturing of steels: a review of achievements and challenges, J. Mater. Sci. 56 (2021) 64–107.

[10] K. Davidson, S. Singamneni, Selective laser melting of duplex stainless steel powders: an investigation, Mater. Manuf. Process. 31 (2016) 1543–1555.

[11] F. Hengsbach, P. Koppa, K. Duschik, M.J. Holzweissig, M. Burns, J. Nellesen, W. Tillmann, T. Tröster, K.P. Hoyer, M. Schaper, Duplex stainless steel fabricated by selective laser melting-Microstructural and mechanical properties, Mater. Des. 133 (2017) 136–142.

[12] K. Saeidi, L. Kevetkova, F. Lofaj, Z. Shen, Novel ferritic stainless steel formed by laser melting from duplex stainless steel powder with advanced mechanical properties and high ductility, Mater. Sci. Eng. 665 (2016) 59–65.

[13] G.N. Nigon, O.B. Isgor, S. Pasebani, The effect of annealing on the selective laser melting of 2205 duplex stainless steel: microstructure, grain orientation, and manufacturing challenges, Opt Laser. Technol. 134 (2021) 106643.

[14] A.D. Iams, J.S. Keist, T.A. Palmer, Formation of austenite in additively manufactured and post-processed duplex stainless steel alloys, Metall. Mater. Trans. 51 (2020) 982–999.

[15] N. Haghdadi, M. Laleh, H. Chen, Z. Chen, C. Ledermueller, X. Liao, S. Ringer, S. Primig, On the pitting corrosion of 2205 duplex stainless steel produced by laser powder bed fusion additive manufacturing in the as-built and post-processed conditions, Mater. Des. 212 (2021) 110260.

[16] N. Haghdadi, P. Cizek, P.D. Hodgson, V. Tari, G.S. Rohrer, H. Beladi, Five-parameter crystallographic characteristics of the interfaces formed during ferrite to austenite transformation in a duplex stainless steel, Phil. Mag. 98 (2018) 1284–1306.

[17] N. Haghdadi, P. Cizek, P.D. Hodgson, Y. He, B. Sun, J.J. Jonas, G.S. Rohrer, H. Beladi, New insights into the interface characteristics of a duplex stainless steel subjected to accelerated ferrite-to-austenite transformation, J. Mater. Sci. 55 (2020) 5322–5339.

[18] Y. Fan, T.G. Liu, L. Xin, Y.M. Han, Y.H. Lu, T. Shoji, Thermal aging behaviors of duplex stainless steels used in nuclear power plant: a review, J. Nucl. Mater. 544 (2021) 152693.

[19] N. Haghdadi, P. Cizek, P.D. Hodgson, H. Beladi, Microstructure dependence of impact toughness in duplex stainless steels, Mater. Sci. Eng. 745 (2019) 369–378.

[20] T.H. Chen, K.L. Weng, J.R. Yang, The effect of high-temperature exposure on the microstructural stability and toughness property in a 2205 duplex stainless steel, Mater. Sci. Eng. 338 (2002) 259–270.

[21] N. Haghdadi, P. Cizek, H. Beladi, P.D. Hodgson, A novel high-strain-rate ferrite dynamic softening mechanism facilitated by the interphase in the austenite/ferrite microstructure, Acta Mater. 126 (2017) 44–57.

[22] G.S. Rohrer, D.M. Saylor, B. El Dasher, B.L. Adams, A.D. Rollett, P. Wynblatt, The distribution of internal interfaces in polycrystals, Z. Metallkd. 95 (2004) 197–214.

[23] M. Miller, K. Russell, G. Thompson, Strategies for fabricating atom probe specimens with a dual beam FIB, Ultramicroscopy 102 (2005) 287–298.

[24] B. Gault, M.P. Moody, J.M. Cairney, S.P. Ringer, Atom Probe Microscopy, Springer Science & Business Media, 2012.

[25] M.S. Moyle, N. Haghdadi, X.Z. Liao, S.P. Ringer, S. Primig, On the microstructure and texture evolution in 17-4 PH stainless steel during laser powder bed fusion: towards textural design, J. Mater. Sci. Technol., accepted, in press.

[26] M. Laleh, A.E. Hughes, M.Y. Tan, G.S. Rohrer, S. Primig, N. Haghdadi, Grain boundary character distribution in an additively manufactured austenitic stainless steel, Scripta Mater. 192 (2021) 115–119.

[27] M. Moyle, C. Ledermueller, Z. Zou, S. Primig, N. Haghdadi, Multi-scale characterisation of microstructure and texture of 316L stainless steel manufactured by laser powder bed fusion, Mater. Char. 184 (2022) 111663.

[28] S.A. David, J.M. Vitek, R.W. Reed, T.L. Hebble, Effect of Rapid Solidification on Stainless Steel Weld Metal Microstructures and its Implications on the Schaeffler Diagram. No. ORNL/TM-10487, Oak Ridge National Lab., TN (USA), 1987.

[29] Y. Sun, R.J. Hebert, M. Aindow, Non-metallic inclusions in 17-4PH stainless steel parts produced by selective laser melting, Materials Des140 (2018) 153–162.

[30] Z. Sun, X. Tan, S.B. Tor, W.Y. Yeong, Selective laser melting of stainless steel 316L with low porosity and high build rates, Mater. Des. 104 (2016) 197–204.

[31] X.Y. Zhang, Q. Zhou, K.H. Wang, Y. Peng, J.L. Ding, J. Kong, S. Williams, Study on microstructure and tensile properties of high nitrogen Cr-Mn steel processed by CMT wire and arc additive manufacturing, Mater. Des. 166 (2019) 107611.

[32] V.A. Hosseini, L. Karlsson, Physical and kinetic simulation of nitrogen loss in high temperature heat affected zone of duplex stainless steels, Materialia 6 (2019) 100325.

[33] Y. Zhao, Y. Sun, X. Li, F. Song, In-situ observation of δ↔ γ phase transformations in duplex stainless steel containing different nitrogen contents, ISIJ Int. 1 (2017) 1–8.

[34] V.A. Hosseini, S. Wessman, K. Hurtig, L. Karlsson, Nitrogen loss and effects on microstructure in multipass TIG welding of a super duplex stainless steel, Mater. Des. 98 (2016) 88–97.

[35] M.A.V. Bermejo, K.T. Pandian, B. Axelsson, E. Harati, A. Kisielewicz, L. Karlsson, Microstructure of laser metal deposited duplex stainless steel: influence of shielding gas and heat treatment, World Weld 65 (2021) 525–541.

[36] T.L. Starr, K. Rafi, B. Stucker, C.M. Scherzer, International Solid Freeform Fabrication Symposium, in: Controlling phase composition in selective laser melted stainless steels, University of Texas at Austin, 2012.

[37] S.D. Meredith, J.S. Zuback, J.S. Keist, T.A. Palmer, Impact of composition on the heat treatment response of additively manufactured 17-4 PH grade stainless steel, Mater. Sci. Eng. 738 (2018) 44–56.

[38] L. Karlsson, H. Arcini, Low energy input welding of duplex stainless steels, World Weld 56 (2012) 41–47.

[39] I. Alvarez-Armas, S. Degallaix-Moreuil, Duplex Stainless Steels, ISTE Ltd. and John Wiley and Sons, 2009.

[40] N. Pettersson, R.F.A. Pettersson, S. Wessman, Precipitation of chromium nitrides in the super duplex stainless steel 2507, Metall. Mater. Trans. 46 (2015) 1062–1072.

[41] B. Zhang, H. Li, S. Zhang, Z. Jiang, Y. Lin, H. Feng, H. Zhu, Effect of nitrogen on precipitation behavior of hyper duplex stainless steel S32707, Mater. Char. 175 (2021) 111096.

[42] A.S. Zubchenko, σ-phase formation in chromium ferritic steels, Mater Sci Heat Treat 24 (1982) 274–276.

[43] D. Wang, H. Kahn, F. Ernst, A.H. Heuer, "Colossal" interstitial supersaturation in delta ferrite in stainless steels:(II) low-temperature nitridation of the 17-7 PH alloy, Acta Mater. 124 (2017) 237–246.

[44] D. Wang, C.W. Chen, J.C. Dalton, F. Yang, R. Sharghi-Moshtaghin, H. Kahn, F. Ernst, R.E.A. Williams, D.W. McComb, A.H. Heuer, "Colossal" interstitial supersaturation in delta ferrite in stainless steels-I. Low-temperature carburization, Acta Mater. 86 (2015) 193–207.

[45] T. Mukherjee, H.L. Wei, A. De, T. DebRoy, Heat and fluid flow in additive manufacturing–Part II: powder bed fusion of stainless steel, and titanium, nickel and aluminum base alloys, Comput. Mater. Sci. 150 (2018) 369–380.

[46] A.J. Ramirez, S.D. Brandi, J.C. Lippold, Secondary austenite and chromium nitride precipitation in simulated heat affected zones of duplex stainless steels, Sci. Technol. Weld. Join. 9 (2004) 301–313.

[47] X. Zhang, K. Wang, Q. Zhou, J. Ding, S. Ganguly, G. Marzio, D. Yang, X. Xu, P. Dirisu, S.W. Williams, Microstructure and mechanical properties of TOP-TIG-wire and arc additive manufactured super duplex stainless steel (ER2594), Mater. Sci. Eng. 762 (2019) 138097.

[48] M. Gouné, F. Danoix, J. Ågren, Y. Bréchet, C.R. Hutchinson, M. Militzer, G. Purdy, S. van der Zwaag, H. Zurob, Overview of the current issues in austenite to ferrite transformation and the role of migrating interfaces therein for low alloyed steels, Mater. Sci. Eng. R 92 (2015) 1–38.

[49] G.C. Weatherly, W.Z. Zhang, The invariant line and precipitate morphology in Fcc-Bcc systems, Metall. Mater. Trans. 25 (1994) 1865–1874.

[50] Y. Gotoh, M. Uwaha, Geometrical Interpretation of the Interfacial Energy between bcc and fcc lattices and preferred orientation relationship of the epitaxy, Jap J App Phys 26 (1987) 17–20.

[51] M. El Hajjaji, These de Doctorat d'Etat, Universite Claude Bernard-Lyon I, 1986.

[52] B. Mills, M. McLean, E.D. Hondros, Surface-energy anisotropy of 3 percent Si-Fe, Philos. Mag. A 27 (1973) 361–368.

[53] M.C. Marinelli, A. El Bartali, J.W. Signorelli, P. Evrard, V. Aubin, I. Alvarez-Armas, S. Degallaix-Moreuil, Activated slip systems and microcrack path in LCF of a duplex stainless steel, Mater. Sci. Eng. 509 (2009) 81–88.

[54] S. Karnati, A. Khiabani, A. Flood, F. Liou, J.W. Newkirk, Proceedings of the 29th Annual International Conference, in: Characterization of impact toughness of 304L stainless steel fabricated through laser, powder bed fusion process, solid freeform fabrication, 2018.

[55] G.E. Dieter, D.J. Bacon, Mechanical Metallurgy, 3, McGraw-hill, New York, 1986.

[56] X.L. Yang, Y.B. Xu, X.D. Tan, D. Wu, Influences of crystallography and delamination on anisotropy of Charpy impact toughness in API X100 pipeline steel, Mater. Sci. Eng. 607 (2014) 53–62.

[57] S. Ukai, W. Izawa, N. Oono, S. Hayashi, Y. Kohno, S. Ohtsuka, T. Kaito, Charpy impact property related to {100} cleavage fracture in 15CrODS steel, Mater. Sci. Technol. 30 (2014) 1709–1714.

[58] J. Chen, F.T. Dong, Z.Y. Liu, G.D. Wang, Grain size dependence of twinning behaviors and resultant cryogenic impact toughness in high manganese austenitic steel, J. Mater. Res. Technol. 10 (2021) 175–187.